

Supplementary Material for

Shaken and Stirred: Oscillatory Segmented Flow for Controlled Size-Evolution of Colloidal Nanomaterials

Milad Abolhasani ^a, Ali Oskooei ^a, Anna Klinkova ^b, Eugenia Kumacheva ^{b,c} and Axel Günther ^{a,c} *

^a Department of Mechanical and Industrial Engineering, University of Toronto, Toronto, ON, M5S 3G8, Canada. Tel: (416)978-1282; E-mail: axel.guenther@utoronto.ca

^b Department of Chemistry, University of Toronto, Toronto, ON, M5S 3H6, Canada. Tel: (416)978-3576; E-mail: ekumache@chem.utoronto.ca

^c Institute of Biomaterials & Biomedical Engineering, University of Toronto, 164 College Street, Toronto, Ontario, M5S 3G9, Canada.

S-1 Long Term Oscillatory Segmented Flow

Oscillatory segmented flow motion of a nitrogen plug and mineral oil segment over a 24 hr period is shown in Fig. S1.

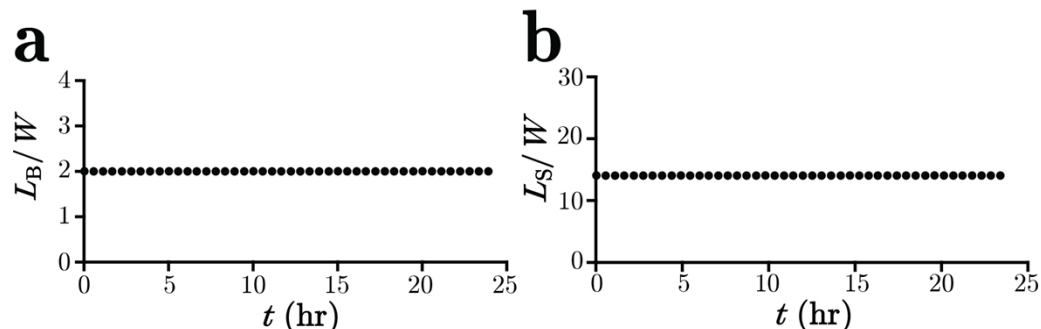


Figure S1. Experimental results for time-evolution of (a) dimensionless nitrogen plug length and (b) dimensionless mineral oil segment length during 24 hours (86,400 oscillation cycles) using device 1. $f=1\text{Hz}$, $P_{0\text{H}}=8.96\text{ kPag}$ and $P_{0\text{L}}=0.0\text{ kPag}$.

S-2 Frequency Spectra of the Oscillatory Segmented Flow

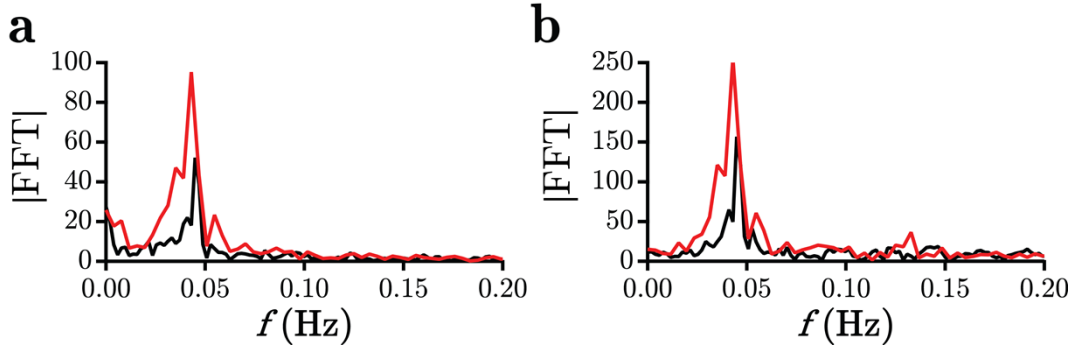


Figure S2. Frequency spectra of the harmonic (a) displacement and (b) velocity plots associated with plots in Figure 3d and 3e. (—) $f=0.5$ Hz, $P_{0H}=14.48$ kPag, $P_{0L}=12.41$ kPag; (—) $f=0.5$ Hz, $P_{0H}=14.48$ kPag, $P_{0L}=6.89$ kPag. 300 images with $dt=0.1$ were used for each experiment.

S-3 Two -Dimensional Numerical Simulation

We developed a two-dimensional numerical model using a numerical finite element program (Comsol 4.3, Comsol Inc., Burlington, MA) that allowed us to study mixing of two miscible liquids in oscillatory segmented flow within a non-inertial frame of reference (attached to the liquid segment). Owing to the small (~ 0.08) Reynolds number, Re , associated with the oscillatory segmented flows studied here, the effect of inertial forces compared to the viscous forces were assumed to be negligible. Our multiphysics model involved a coupled laminar fluid flow and the transport of a dilute species. It numerically solves the continuity equation,

$$\frac{\partial \rho}{\partial t} + \nabla(\rho u) = 0, \quad \text{in combination with the Navier-Stokes equation,}$$

$\rho \frac{\partial u}{\partial t} + \rho(u \nabla) u = \nabla[-pI + \tau] + F$, to predict the velocity field inside the liquid segment. Symbol

ρ is the liquid density, u is the velocity vector, p is the pressure, F is the volume force vector,

$\tau = 2\mu Z - \frac{2}{3}\mu(\nabla \cdot u)I$ is the viscous stress, and $Z = \frac{1}{2}(\nabla u + (\nabla u)^T)$ is the strain rate tensor.

Continuity equation for incompressible flow reduces to $\rho \nabla \cdot u = 0$, and the Navier-Stokes equation becomes, $\rho \frac{\partial u}{\partial t} + \rho(u \nabla) u = \nabla[-pI + \mu(\nabla u + (\nabla u)^T)] + F$.

Figures S3a and S3b show the boundary conditions of the two-dimensional computational domain and the corresponding streamlines of the axisymmetric recirculation zones, respectively.

In our numerical model, gas plugs were kept stationary while the top and the bottom walls were periodically moving with the gas plug velocity (i.e., a moving wall in the reference frame). To model the oscillatory motion of the liquid segment, a harmonic velocity profile was imposed on the top and bottom microchannel walls, with a frequency of $f=1/T$, a period T and an amplitude of a . The Capillary number is defined as $Ca=\mu U/\sigma$, where μ is the liquid viscosity and σ is the interfacial tension between the gas and liquid. At the fluid velocities considered in this study, $Ca < 0.01$. A film of uniform thickness $\delta=0.02 \times 300 \text{ } \mu\text{m} = 6 \text{ } \mu\text{m}$, equal to 2% of the microchannel hydrodynamic diameter⁴⁶, was assumed to separate the gas plugs from the top and bottom microchannel walls.

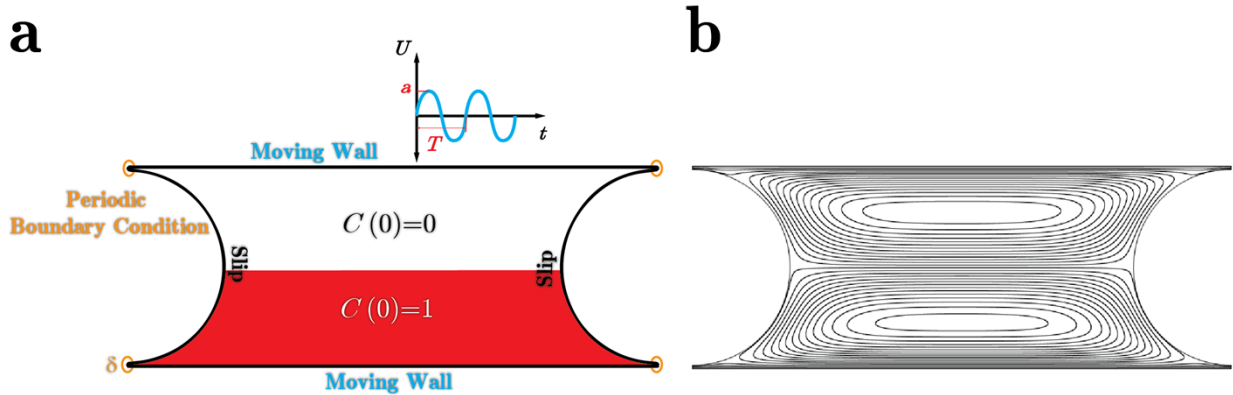


Figure S3. (a) Schematic illustration of the two-dimensional computational domain and boundary conditions used in the numerical simulation, and (b) the corresponding streamlines.

A slip boundary condition was used at the front and back ends of the liquid segment, where the segment was in contact with a cap of a gas plug. The slip wall boundary condition assumes there are no viscous effects at the wall, i.e., $u \cdot n = 0$ and $(-pI + \mu(\nabla u + (\nabla u)^T))n = 0$. A periodic boundary condition that assumes the fluid leaving the domain through the liquid films at the right side of the computational domain enters the domain through the liquid films at the left side was used as the boundary condition for velocity and pressure at the liquid films in the single-phase laminar flow module.

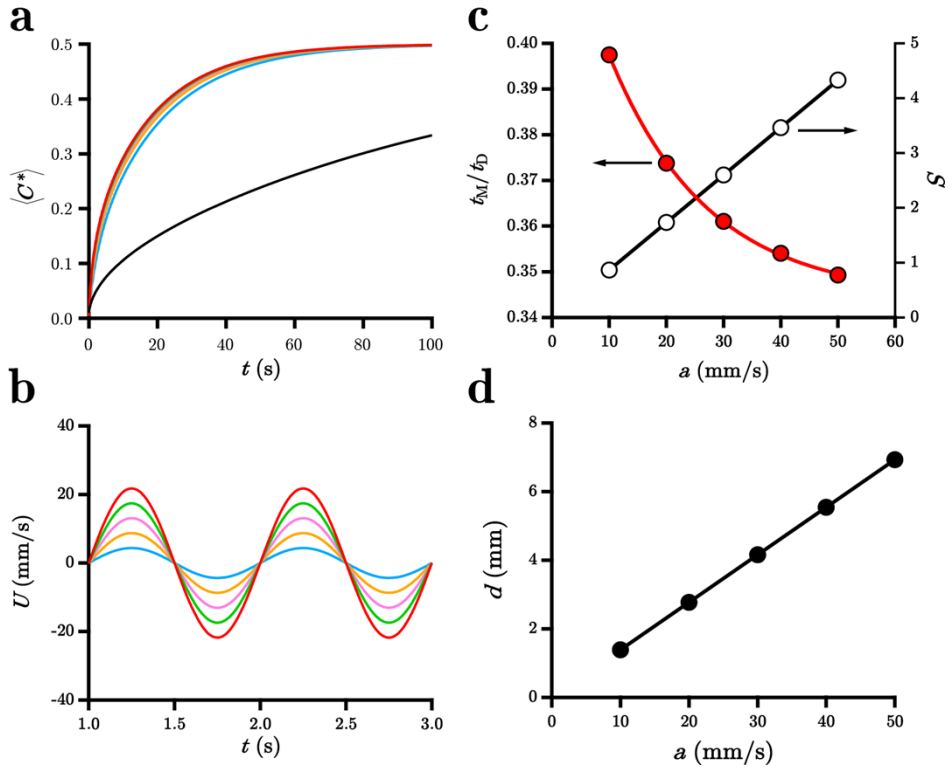


Figure S4. (a) Numerically predicted evolution of time-dependent solute concentration that was spatially averaged across the top half of the liquid segment: $f=1\text{Hz}$, $L_S/W=2$, $D=1\text{e}-11\text{ m}^2/\text{s}$, (●) $a=0$, (●) $a=10\text{ mm/s}$, (●) $a=20\text{ mm/s}$, (●) $a=30\text{ mm/s}$, (●) $a=40\text{ mm/s}$ and (●) $a=50\text{ mm/s}$. (b) Velocity magnitude evolution of the center position of the liquid segment. (c) Normalized mixing time and stirring strength for different velocity amplitudes. (d) Total distance traveled by the liquid segment in one complete oscillation cycle for different velocity amplitudes.

The convection-diffusion equation, $\frac{\partial c}{\partial t} + u\nabla c = \nabla(D\nabla c)$, was numerically solved to obtain the

concentration distribution inside the top and bottom halves of the liquid segment during the oscillatory segmented flow-based mixing process. Symbols c and D are the concentration and diffusivity of the solute molecules, respectively.

A two-step solver was used to solve the above-mentioned model. First, a transient solver was used to solve the single-phase laminar flow module and find the velocity distribution inside the liquid segment at the specified time. In the second step, the velocity vector calculated in the first step was employed as the input velocity vector of the convection-diffusion equation and another time-dependent solver was used to evaluate the time-resolved average concentration evolution of the solute molecules inside the liquid segment. An unstructured mesh was generated with the resolution of the narrowest region of 12 elements, resulting in 1,860,889 elements. The properties of light mineral oil ($\rho=838\text{ kg/m}^3$, $\mu=21.1\text{ mPa.s}$), were used in the model.

Figure S4a shows the normalized average solute concentration inside the top half of the segment for the same liquid segment length, the same oscillation frequency and different velocity amplitudes. Figure S4b, illustrates the velocity evolution of the center of the liquid segment during the oscillatory segmented flow. The mixing times associated with the average concentration plots in Fig. S4a were evaluated under the same criteria that were mentioned in section 2.1 for the experimental case (Fig. S4c). As shown in Fig. S4c, increasing the velocity amplitude increased the stirring strength and total displacement of the liquid segment (Fig. S4d) and decreases the mixing time. The improved mixing time with the increased displacement of the liquid segment is consistent with the experimental results presented in section 3.2.

S-4 Mixing Time Evolution for Different Oscillation Frequencies

Figure S5 shows the experimentally measured mixing times normalized by the diffusion time for the same L_S , P_{0H} , P_{0L} and different oscillation frequencies between 0 and 50 Hz. As explained in the manuscript, section 3.2, the mixing time is governed by the total displacement of the liquid segment during one unit time (1s). As discussed in the manuscript, section 3.2, we attribute the behavior of the mixing time, shown in Fig. S5, to the variation of the total liquid segment displacement over the unit time (1s). As the total liquid segment displacement over the unit time increases (up to 3Hz), owing to the increased number of full recirculations within the liquid segment, the mixing time decreases, however further increasing the oscillation frequency (after 3Hz) due to the decreased total displacement of the liquid segment over the unit time (i.e., decreased contribution of convective mixing) increases the mixing time.

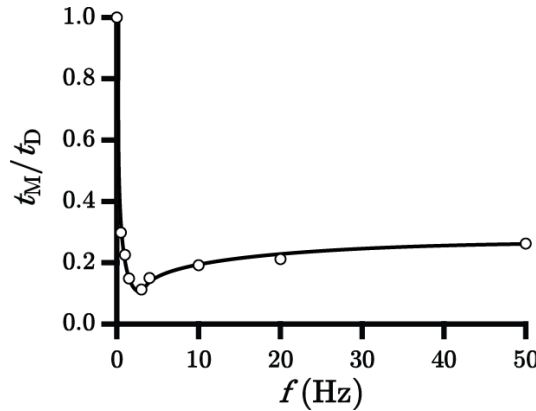


Figure S5. Frequency dependency of normalized mixing time for $L_S = 1.2 \pm 0.1$ mm, $P_{0H} = 8.96$ kPag, and $P_{0L} = 0.0$ kPag.

S-5 Characterization of the Oscillatory Motion

The displacement distance and velocities of the center position of a liquid segment and their corresponding frequency spectra during the oscillatory mixing process for different frequencies are shown in Figs. S6 and S7, respectively. The response time of the liquid segment velocity to the applied pressure change, t_{RT} , is shown in Fig. S6c and was evaluated from 1800 image frames acquired at $dt=33.3$ ms.

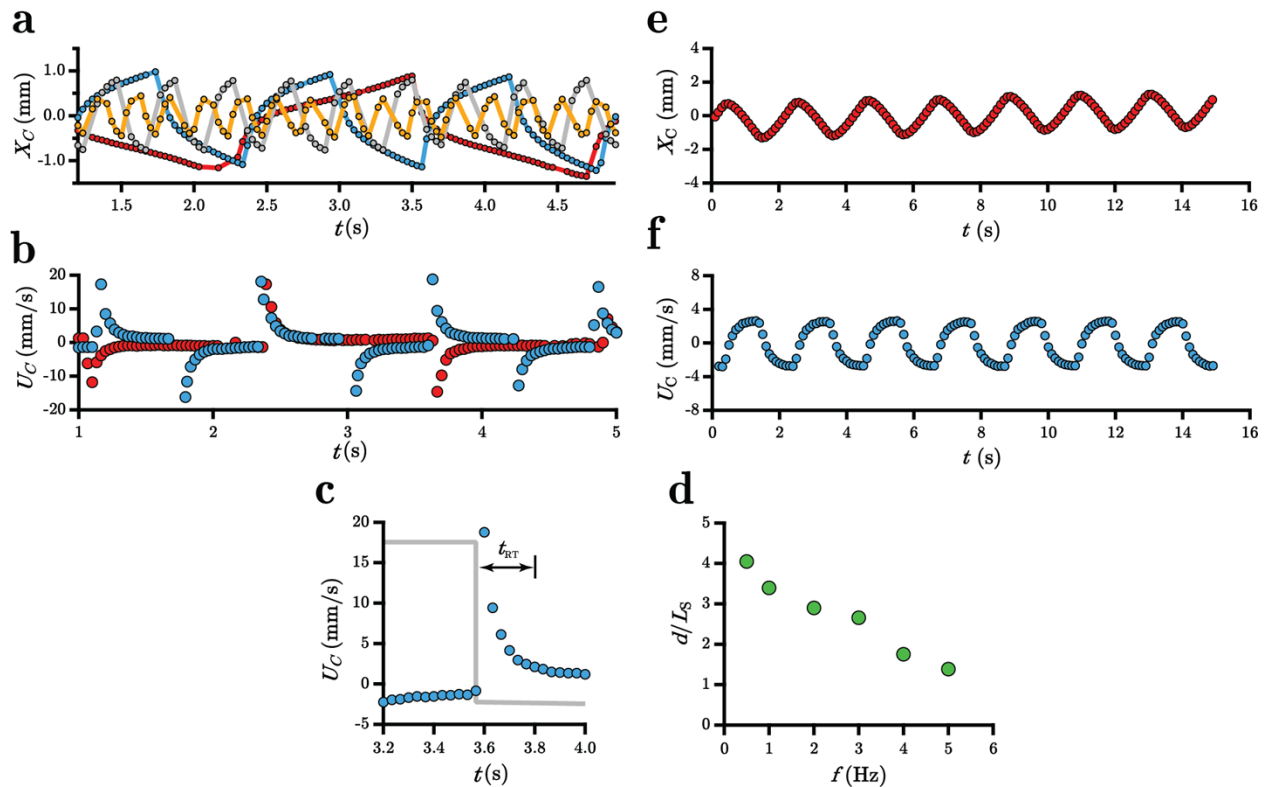


Figure S6. (a) Liquid segment center point displacement and (b) center point velocity for a liquid segment with $L_S = 1.2 \pm 0.1$ mm, $P_{0H} = 8.96$ kPag and $P_{0L} = 0.0$ kPag plotted for frequencies: (●) $f=0.5$ Hz, (●) $f=1$ Hz, (●) $f=3$ Hz and (●) $f=5$ Hz. (c) Velocity response time for a liquid segment with $L_S = 1.23$ mm, $P_{0H} = 8.96$ kPag, $P_{0L} = 0.0$ kPag and $f=1$ Hz. (d) Total distance traveled by the liquid segment in one complete oscillation cycle plotted against corresponding oscillation frequency. Displacement and velocity plots were computed for a sequence of 1800 images (30 frames per second).(e) Modified liquid segment center point displacement and (f) center point velocity for $L_S = 1.9 \pm 0.1$ mm $P_{0H} = 17.24$ kPag, $P_{0L} = 0.0$ kPag and $f=1$ Hz in a modified setup. All experiments were conducted in device 1, using mineral oil-helium pair.

The total displacement of the liquid segment over one oscillation cycle for different oscillation frequencies is shown in Fig. S6d. The initial jumps of the liquid segment displacement and

velocities, shown in Figs. S6a and S6b, are associated with the solenoid valves and PID settings of the digital servo pressure controllers utilized in this study. As the electromagnetic valve switched from the atmospheric pressure to the pre-determined pressure level of the digital servo pressure controller, the solenoid valve of the regulator opened to allow more gas to enter the tubing upstream of the microfluidic device, as well as the gas-filled channel network on the device. The regulator then adjusts the state of the valve to keep the pressure at the pre-determined value. The initial opening state of the solenoid valve results in a pressure slightly larger (~ 2 kPa) than the target pressure, with an initial pressure that overshoots as compared to the target square wave profile. As a result, the initial displacement of the liquid segments is more rapid as shown in Figs. S6a and S6b.

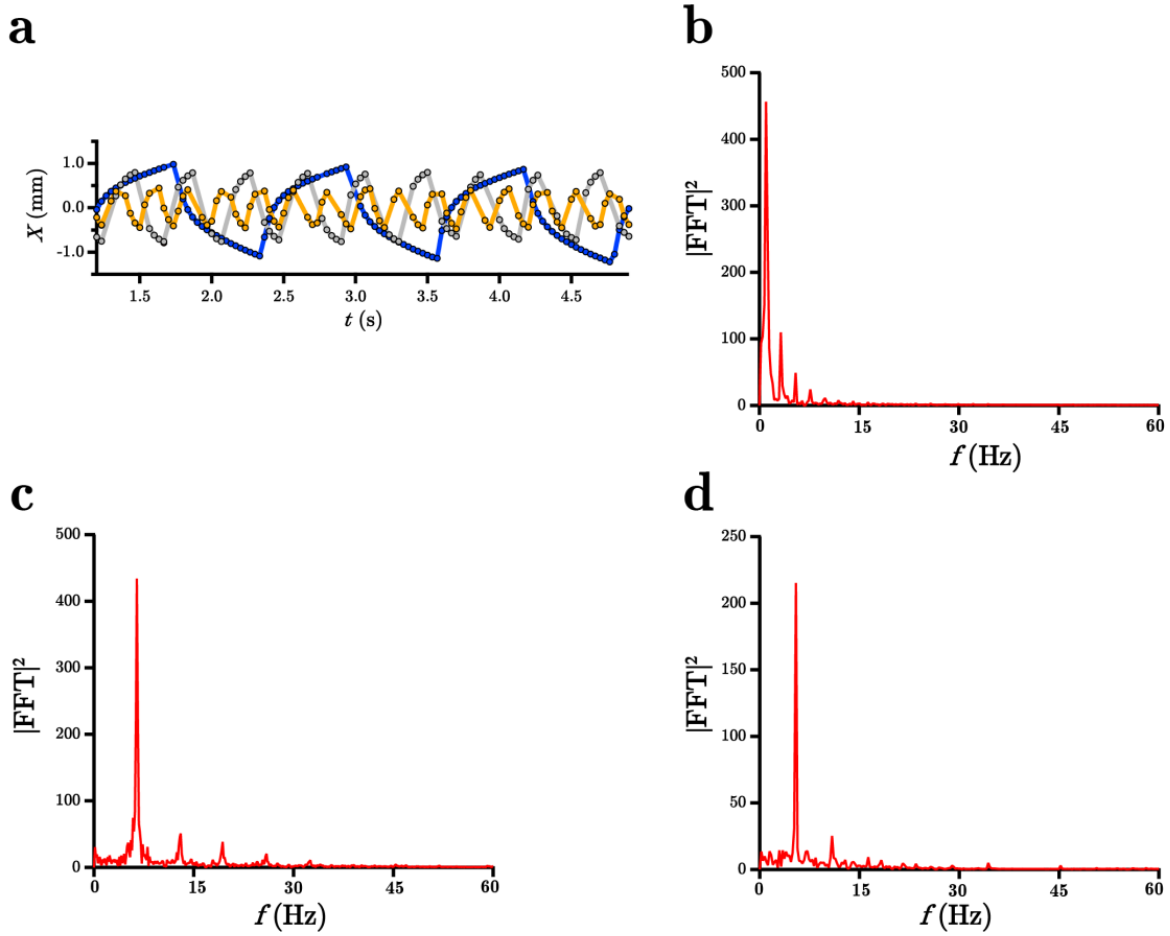


Figure S7. (a) Experimental results for periodic displacement of liquid segment center point for fixed parameters $L_S = 1.2 \pm 0.1$ mm, $P_{0H} = 8.96$ kPag and $P_{0L} = 0.0$ kPag: (●) $f = 1$ Hz, (●) $f = 3$ Hz and (●) $f = 5$ Hz. Frequency spectra of the displacement curves in (a) for (b) $f = 1$ Hz, (c) $f = 3$ Hz and (d) $f = 5$ Hz. All experiments were conducted in device 1, using mineral oil-helium pair.

In order to impose a pressure profile that more closely matches the square wave, either the PID settings of the digital servo pressure controller need to be adjusted or a large capacitance (e.g., a gas reservoir with the volume ratio of 5 to 1 compared to the tubings and microfluidic device volume) needs to be added between the digital servo pressure controller and the electromagnetic valve to dampen the effect of switching between the atmospheric pressure and P_{0H} value. Figures S6e and S6f show the displacement and velocity profiles of the center of the liquid segment for a modified actuation setup, including two 20 mL gas reservoirs between the digital servo pressure controllers and the electromagnetic valves. Smoother displacement and velocity profiles were obtained that do not display the previously observed initial jump.

Moreover, the large void fraction (0.55-0.7) occupied by the gas plugs resulted in an actuation time delay between the segments more proximal to the actuation sources as compared to the more distal location in the microchannel center, see Movie M6. Figure S7 shows the displacement of two liquid segments, one located close to the inlet actuation source (i.e., 0.05 m from the T-junction) and one at the center of the microchannel (i.e., 0.35m from the T-junction). A liquid segment closer to the actuation source experiences the increased pressure change faster than a liquid segment further in the center of the microchannel. We attribute this time delay to the compressibility of the gas, and the travel time of the pressure wave across the train of gas plugs. As shown in Fig. S7, owing to the viscous friction and compressibility of the gas, the amplitude of the liquid segment displacement reduces towards the center region of the microchannel.

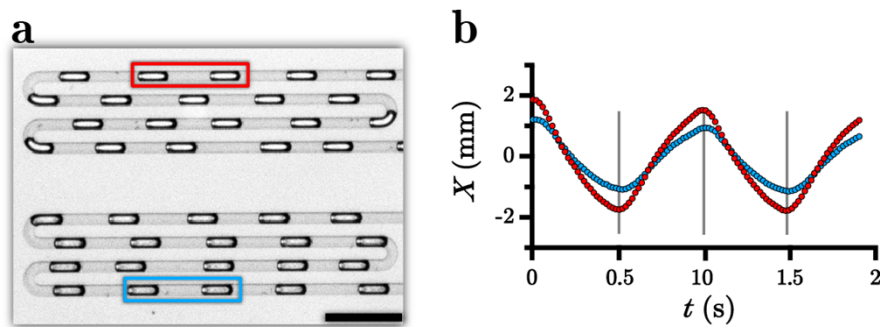


Figure S8. (a) Bright-field image of ethanol-nitrogen segmented flow formed in a silicon-based microfluidic device. Two liquid segments located at (●) 0.05 m and (●) 0.35 m downstream of the T-junction are highlighted. Scale bar is 2 mm. (b) Corresponding center point displacements of the liquid segments highlighted (a) with $L_{S/w}=4$, $P_{0H}=12.41$ kPag, $P_{0L}=8.96$ kPag and $f=1$ Hz.

S-6 On-chip UV-Vis Spectroscopy

Schematic of the experimental setup, utilized for on-chip monitoring of gold nanorods etching process and the raw UV-Vis absorbance signal of gold nanorods solution within a liquid segment trapped between two inert gas plugs are shown in Figs. S9 and S10, respectively.

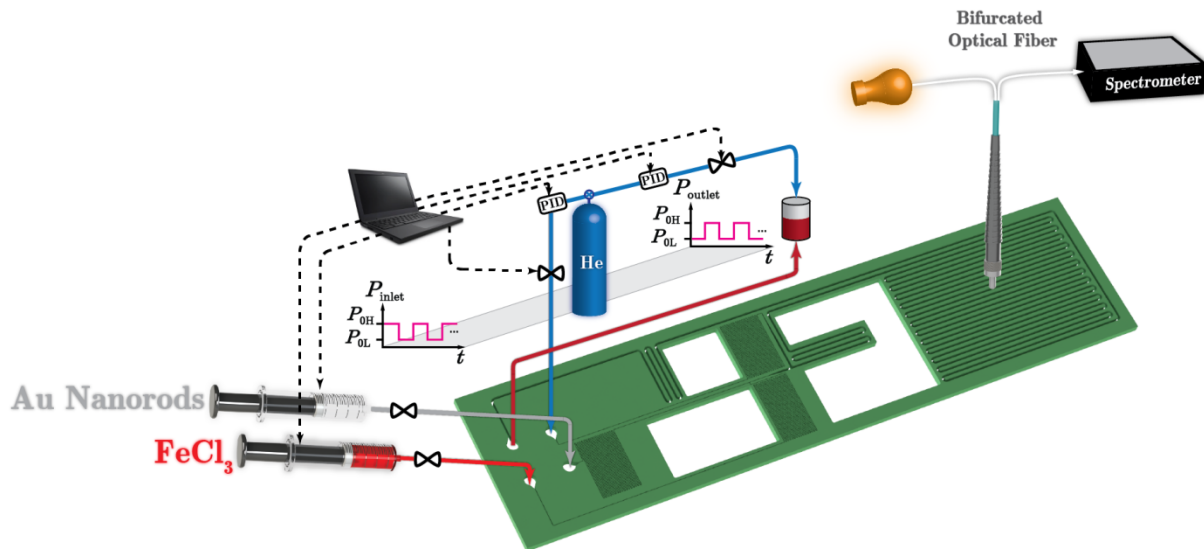


Figure S9. Schematic of the oscillatory segmented flow platform integrated with a bifurcated fiber for on-chip monitoring of gold nanorod UV-Vis absorption spectra during the etching process.

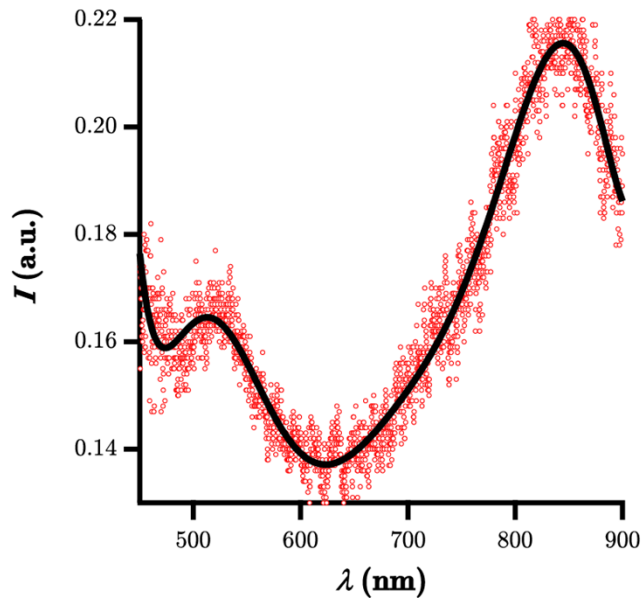


Figure S10. (a) Raw on-chip UV-Vis absorption signal detected by the miniature spectrometer along with its 9th order polynomial fit with an R-square of 0.96 for a gold nanorod solution with an off-chip OD of 0.6.

Movies

Movie M-1 Oscillatory segmented flow of nitrogen plugs within ethanol. $f=0.5$ Hz, $P_{0H}=14.48$ kPag, and $P_{0L}=6.89$ kPag.

Movie M-2 Oscillatory segmented flow mixing of transparent and fluorescently labelled mineral oils entrapped between helium plugs. $f=1$ Hz, $P_{0H}=8.96$ kPag, and $P_{0L}=0.0$ kPag.

Movie M-3 Oscillatory segmented flow mixing of transparent and fluorescently labelled mineral oils entrapped between helium plugs. $f=4$ Hz, $P_{0H}=8.96$ kPag, and $P_{0L}=0.0$ kPag.

Movie M-4 Oscillatory segmented flow mixing of transparent and fluorescently labelled mineral oils entrapped between helium plugs. $f=10$ Hz, $P_{0H}=8.96$ kPag, and $P_{0L}=0.0$ kPag.

Movie M-5 Two-dimensional numerical simulation of the oscillatory mixing $f=2$ Hz

Movie M-6 Spectral characterization of gold NRs during the etching process using oscillatory segmented flow with $f=1$ Hz and $L_s=2.5$ mm.

Supplemental Reference

1. Fries, D. M.; Trachsel, F.; von Rohr, P. R., Segmented gas–liquid flow characterization in rectangular microchannels. *International Journal of Multiphase Flow* 2008, **34**, (12), 1108-1118